INTERNATIONAL JOURNAL FOR NUMERICAL METHODS IN FLUIDS
Int. J. Numer. Meth. Fluids 2007; **54**:1–28
Published online 8 November 2006 in Wiley InterScience (www.interscience.wiley.com). DOI: 10.1002/fld.1389

Using vorticity to define conditions at multiple open boundaries for simulating flow in a simplified vortex settling basin

A. N. Ziaei[1,*,†], J. M. McDonough[2], H. Emdad[3] and A. R. Keshavarzi[1]

[1]*Water Engineering Department, Shiraz University, Shiraz, Iran*
[2]*Departments of Mechanical Engineering and Mathematics, University of Kentucky, Lexington, Kentucky*
[3]*Mechanical Engineering Department, Shiraz University, Shiraz, Iran*

SUMMARY

In this paper a method is developed to define multiple open boundary (OB) conditions in a simplified vortex settling basin (VSB). In this method, the normal component of the momentum equation is solved at the OBs, and tangential components of vorticity are calculated by solving vorticity transport equations only at the OBs. Then the tangential vorticity components are used to construct Neumann boundary conditions for tangential velocity components. Pressure is set to its ambient value, and the divergence-free condition is satisfied at these boundaries by employing the divergence as the Neumann condition for the normal-direction momentum equation. The 3-D incompressible Navier–Stokes equations in a primitive-variable form are solved using the SIMPLE algorithm. Grid-function convergence tests are utilized to verify the numerical results. The complicated laminar flow structure in the VSB is investigated, and preliminary assessment of two popular turbulence models, k–ε and k–ω, is conducted. Copyright © 2006 John Wiley & Sons, Ltd.

Received 15 May 2006; Revised 20 September 2006; Accepted 22 September 2006

KEY WORDS: open boundary; primitive variables; vortex settling basin; turbulence modelling

1. INTRODUCTION

Swirling flow patterns in hydrocyclones are often used to separate solid from liquid in industrial processes. A vortex settling basin (VSB) is a similar device that uses vortices induced in a cylindrical basin/chamber to efficiently extract sediment from diverted water of a river. In a VSB, flow is introduced tangentially into a cylindrical basin having an orifice at the centre of its bottom.

*Correspondence to: A. N. Ziaei, Water Engineering Department, Shiraz University, Shiraz, Iran.
†E-mail: ali.ziaei@uky.edu

Contract/grant sponsor: Shiraz University, University of Kentucky Center for Computational Sciences, University of Kentucky Computing Center

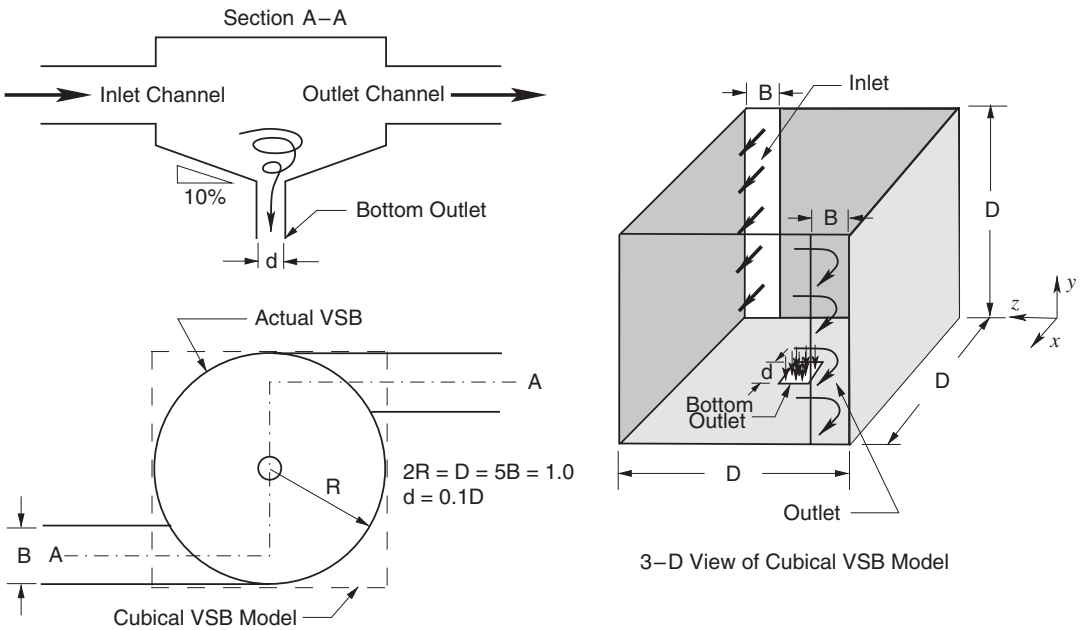

Figure 1. Schematic diagram of a vortex settling basin (left) and the simplified model (right).

The combined vortex (combination of free and forced vortices) causes sediment particles which are heavier than water to move towards the periphery of the chamber due to centrifugal force. Secondary flows (Rea [1]) move the fluid layer near the basin floor toward the central orifice (Athar *et al*. [2]). Since the sediment particles move with the flow along a helical path, they have a settling length that is longer than the basin dimensions. This feature makes the VSB more efficient than ordinary settling tanks. A small fraction (about 10%) of inlet flow leaves the domain from the bottom outlet, and the rest which carries low sediment load exits through an outlet channel as shown on the left-hand side of Figure 1.

Elaborate studies have been made on different properties of the VSB mostly by physical modelling. These have emphasized improving efficiency through changing the VSB geometric configuration and obtaining empirical formulas for design purposes. Paul *et al*. [3] surveyed different configurations of the VSB briefly and presented a new configuration to improve the removal efficiency. Athar *et al*. [4] presented some formulas to estimate the removal efficiency based on VSB dimensions and flow properties. Velocity variation within the VSB was also investigated in different studies. Athar *et al*. [2] measured velocity components in a VSB; they showed that flow patterns are different in different segments of the vortex chamber, and inlet and outlets cause the flow to deviate from a Rankine vortex. Investigation of swirling flow in a hydrocyclone also showed that the flow is highly turbulent and three-dimensional (Nowakowski *et al*. [5]). Hence, three-dimensional numerical simulation is essential to model the VSB with reasonable accuracy.

The multiphase flow (water, air and sediment particles) in a VSB is very complicated, and in the present paper, which is part of an ongoing program on VSB numerical simulation, the main emphasis will be on defining appropriate boundary conditions in 3-D and studying flow structure

DOI: 10.1002/fld

in single-phase (water) laminar flow. A preliminary assessment of performance of k–ε and k–ω models is also provided for this simplified case.

To perform numerical modelling, the physical domain should be truncated to a finite computational domain. Necessity to truncate the physical domain gives rise to difficulty in defining boundary conditions at so-called open boundaries (OB). The OBs are portions of the boundary at which inflow and outflow may coexist, and defining corresponding open boundary conditions (OBC) is a difficult and important task. These partly depend on the flow outside the computational domain, which is logically unknown; therefore, some artificial boundary conditions that may contain additional information typically must be imposed. Whatever these conditions are, they should be defined such that the numerical model is mathematically well posed, and flow enters and leaves the computational domain without substantial unphysical effect on flow behaviour within the computational domain.

Since these OBCs are not set by nature, they are not uniquely defined. The homogeneous Neumann boundary condition is commonly used at OBs. This type of OBC for the normal velocity component yields an ill-posed problem because of insufficient information for its specification, as indicated by Sani and Gresho [6]. Setting pressure equal to the atmospheric value at OBs fixes the ill-posed problem but sacrifices the divergence free condition on the open boundary (Gresho [7]). OBCs that have gained considerable popularity compared with others are the so-called non-reflecting (NR) boundary conditions that take the following form [7]:

$$\frac{\partial \varphi}{\partial t} + \bar{u}\frac{\partial \varphi}{\partial \mathbf{n}} = 0 \tag{1}$$

Here ϕ is any velocity component, and $\bar{u}$ is a representative value of the normal velocity at the exit. In [6] these boundary conditions were applied for different test cases, and it was shown that results were very case dependent. The homogeneous Neumann boundary condition often leads to poor results for high Reynolds number flows (Shyy [8] and Behr *et al*. [9]). However, none of these OBCs can represent the complicated physics of the VSB outlets. On the other hand, Concha *et al*. [10] point out that the best separation in a hydrocyclone occurs near the formation of a 'rope discharge' which is set by outlet velocity angle at the apex. Therefore, to obtain reasonably accurate results, either the boundaries have to be located far from the area of interest, which increases the computational cost, or a proper technique should be used to define boundary conditions at the outlets so as to replicate this complicated discharge.

There is a class of OBCs based on the stress tensor. These lead to a mathematically well-posed problem, but values for components of this tensor are once again generally unknown, and a zero stress tensor is usually assumed [6]. This kind of OBC has been used frequently to define the boundary conditions at hydrocyclone outlets in the context of the finite element method (Nowakowski and Dyakowski [11], Doby *et al*. [12]).

The velocity–vorticity formulation of the Navier–Stokes (N.–S.) has also gained some favour due to its ability to decouple the momentum and continuity equations. Although in this set of equations, setting OBCs for vorticity is easier, BCs for the velocity components are required to solve the continuity equation [13]. Bertagnolio [13] used vorticity definition to construct Neumann boundary conditions for tangential velocity components at the OBs in the context of a velocity–vorticity formulation.

In the present study a method to construct OBCs for incompressible fluid flow simulations is implemented to solve the 3-D N.–S. equations in primitive-variable form. In this approach, the normal component of the momentum equation is solved at the OBs, and tangential components

DOI: 10.1002/fld

of vorticity are calculated by solving the N.–S. equation in a velocity–vorticity formulation only at the OBs. Then the tangential vorticity components are used as Neumann boundary conditions for tangential velocity components. The continuity equation is employed to define a BC for the normal component of velocity on the first grid cell outside the domain. Backward differencing is used for the vorticity equation wherever it is necessary to avoid introduction of image points. Pressure is set to its ambient value at the OBs. This set of OBCs results in a well-posed problem without invoking any unphysical assumptions, and the divergence-free condition is also satisfied at the OBs. The method is implemented to simulate the flow field in a simplified VSB.

In the remainder of this paper, first the governing equations are recalled, and the boundary conditions based on the definition of vorticity are explained in detail. Then a numerical procedure to utilize this approach is presented at the end of Section 2. The third section is devoted to describing a simplified VSB test case. In the fourth section the laminar flow field within the VSB and its behaviour near the OBs are investigated, and results of two turbulence models are outlined in Section 5. A final section presents conclusions drawn from this study.

2. GOVERNING EQUATIONS AND BOUNDARY CONDITIONS

The general 3-D incompressible N.–S. equations in primitive-variable form in a domain Ω bounded by the Dirichlet portion Γ_D (solid walls and inlets) and the open portion Γ_N are as follows:

$$\frac{\partial \mathbf{u}}{\partial t} + \mathbf{u} \cdot \nabla \mathbf{u} = -\nabla p + \frac{1}{Re} \Delta \mathbf{u} + \mathbf{F} \tag{2}$$

$$\nabla \cdot \mathbf{u} = 0 \tag{3}$$

Here $\mathbf{u}$ is the velocity vector $(u, v, w)^T$, p is the pressure, Re is the Reynolds number and $\mathbf{F}$ is a body force; ∇ and Δ are gradient and Laplace operators, respectively. These equations are subjected to the following boundary conditions:

$$\mathbf{u} = \mathbf{w} \quad \text{on } \Gamma_D \tag{4}$$

where $\mathbf{w}$ is the prescribed velocity vector on the Dirichlet part of the boundary; but boundary conditions for velocity components and pressure on the OBs are usually unknown. Hence, the first aim of this paper is to define an appropriate procedure to compute these values. For sake of simplicity we use a right-handed orthonormal vector basis $(\mathbf{t}_1, \mathbf{t}_2, \mathbf{n})$ for which $\mathbf{t}_1$ and $\mathbf{t}_2$ are tangential to the OBs, and $\mathbf{n}$ is the outward normal vector.

2.1. Tangential velocity component boundary conditions

Bertagnolio [13] used vorticity definition as Neumann boundary conditions for the tangential velocity components in the context of a velocity–vorticity formulation as follows:

$$\frac{\partial u_{t_1}}{\partial \mathbf{n}} = +\omega_{t_2} + \frac{\partial u \cdot n}{\partial \mathbf{t}_1} \quad \text{on } \Gamma_N \tag{5}$$

$$\frac{\partial u_{t_2}}{\partial \mathbf{n}} = -\omega_{t_1} + \frac{\partial u \cdot n}{\partial \mathbf{t}_2} \quad \text{on } \Gamma_N \tag{6}$$

DOI: 10.1002/fld

where u_{t_1}, u_{t_2}, ω_{t_1} and ω_{t_2} are tangential velocity and vorticity components, respectively. These equations can be easily used as boundary conditions for the tangential velocity components to solve the N.–S. equations expressed in primitive variables provided that the vorticity components are available at the outflow boundaries. To calculate these, the vorticity component transport equations should be solved at the OBs. We remark that it is easy to show that the combination of Equations (5) and (6) and use of ω obtained from the vorticity transport equation automatically collapses to the conditions for fully developed flow if the velocity field exhibits such features.

2.2. *Vorticity transport equation*

Taking the curl of Equation (2) yields the following vorticity transport equation:

$$\frac{\partial \boldsymbol{\omega}}{\partial t} + \nabla \cdot (\mathbf{u}\boldsymbol{\omega}) = \frac{1}{Re} \Delta \boldsymbol{\omega} + \nabla \times \mathbf{F} \tag{7}$$

where $\boldsymbol{\omega}$ is the vorticity vector. Solving this equation in both t_1 and t_2 directions provides the required vorticity components at OBs. Notice that no explicit boundary condition is necessary to solve Equation (7) except vorticity definition as the curl of the velocity vector, which is calculated from velocity components obtained at a previous iteration or time step in the interior of Ω. Backward differencing is necessary to avoid evaluating vorticity components outside the domain, details of which are presented in the next section. Since the equations are solved in an iterative procedure, in the first iteration the vorticity values are calculated based on initial values of the velocity components at the OBs.

2.3. *Boundary condition for pressure and normal component of velocity*

So far the boundary conditions for the tangential velocity components have been introduced. However, boundary conditions for the normal component of velocity and pressure must be prescribed.

The momentum equation in the normal direction is solved to obtain the normal velocity component at the OBs. The spatial discretization of this equation introduces a value of the normal velocity component outside the domain (at an image point, Figure 2) both through the diffusive and convective terms. This might be handled by neglecting diffusion normal to the boundary and using a first-order upwind scheme for convective terms in the normal direction. These approximations result in an equation that is very similar to the NR boundary conditions often used to derive unknown values at the OBs despite the fact that such an approximation does not completely represent the physics. Another alternative, used in the current study, is implementing the continuity equation at the OB to obtain the normal velocity component at the image point. With this method the normal velocity component is defined so that the divergence-free condition is satisfied at the OBs. Therefore, pressure can be set to zero (or any appropriate ambient value consistent with incompressible flow) without any damage to the divergence-free requirement at the OBs while maintaining well posedness of the elliptic problem for pressure. We emphasize that in contrast to the true physical situation shown in Figure 1, our simplified model contains no exterior ducting or piping extending beyond the outlet planes. Hence, the outlet flow immediately encounters ambient pressure. This is the case for some VSB configurations where flow exits the basin over a spill weir at the beginning of an outlet channel (see e.g. [3]).

DOI: 10.1002/fld

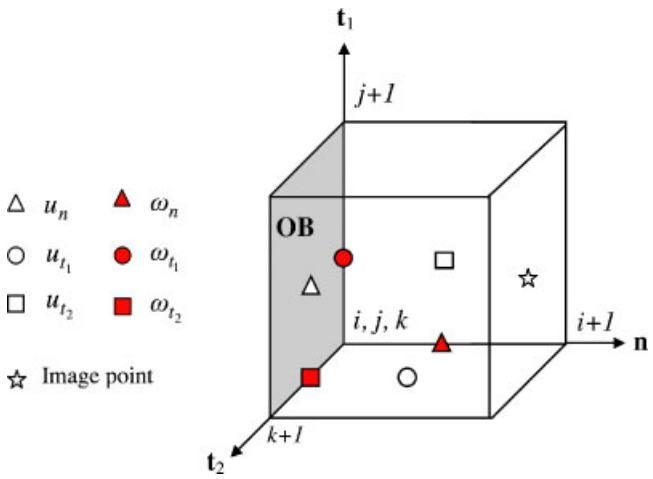

Figure 2. Typical grid cell on an outflow boundary.

2.4. Numerical procedure

The conservation form of the N.–S. equations in both primitive and velocity–vorticity formulations are discretized on a structured staggered grid (Figure 2) using a finite-volume approach. The staggered grid provides a consistent and easy way to calculate vorticity components in the velocity–vorticity formulation as shown by Liu [14]. At a solid boundary (i.e grid points at the end of a solid boundary and beginning of an outflow boundary) the vorticity components must be calculated using the definition of vorticity. For instance, at the bottom surface shown in Figure 2, corresponding to $t_1 = 0$

$$\omega_{t_1} = 0 \tag{8}$$

$$\omega_{t_2} = -\frac{\partial u_{\mathrm{n}}}{\partial t_1} \tag{9}$$

To evaluate tangential vorticity components at a face corresponding to an image point, backward differencing is necessary to prevent introduction of velocity values outside the domain. For example, at the image point shown in Figure 2 we have

$$\omega_{t_2}(i+1, j, k) = \left(\frac{u_{t_1}(i, j, k) - u_{t_1}(i-1, j, k)}{\Delta x_{\mathrm{n}}}\right) - \left.\frac{\partial u_{\mathrm{n}}}{\partial t_1}\right|_{i+1, j, k} \tag{10}$$

where Δx_{n} is grid spacing in the normal direction. The required normal velocity component at the image point is calculated using the continuity equation which is applied on the typical boundary cell shown in Figure 2.

Power-law and centred-difference schemes are used to treat convective and diffusive terms, respectively. The QUICK scheme is also available to treat convective terms in interior grid cells. The SIMPLE algorithm of Patankar [15] is used to solve the steady dimensionless N.–S. equations. The two tangential vorticity transport equations are solved only at the OB after performing the velocity correction step in the SIMPLE procedure; then the boundary conditions are updated.

DOI: 10.1002/fld

3. A SIMPLIFIED VORTEX SETTLING BASIN PROBLEM

In a basic VSB configuration both inlet and outlet channels are kept in alignment following a straight line tangent to the vortex chamber. In [3] it is shown that for this case, a deflector (a C-shaped plate covering one half of the basin periphery) is necessary to improve the removal efficiency, especially for fine sediment particles. Though the deflector increases the residence time—a positive effect, it also decreases the strength of secondary flows, which is not satisfactory (Chrysostomou [16]). Paul *et al*. [3] recommended a configuration utilizing a counter-clockwise vortex which is more efficient for coarser sediment particles and obviates the need for a deflector. The experimental study by Ziaei [17] also indicated that in this counter-clockwise condition, no sediment particles remained on the basin floor. However, the resulting central vortex is more complicated because the axis of the air core makes an angle with the vertical direction and is displaced with respect to the centre of the orifice due to inlet and outlet channel flows; hence, the flow is not axisymmetric with respect to the vertical direction. In [4] it is shown that a configuration such as depicted in Figure 1 is the most efficient form of VSB device. In this type, a straight inlet channel joins the vortex chamber tangentially at one side, and the outlet channel is connected tangentially at the point that is diametrically opposite to the junction of the inlet channel; the resulting vortex is rotating in a counterclockwise direction. Notice that this is due to geometry and not because of the vortex circulation direction, per se.

In the present study, we simulate the flow field in a simplified cubic VSB model (unity side length) with a counter-clockwise vortex caused by a bottom drain port and opposing inlet and outlet channels. For sake of simplicity, the free surface between air and water that is an intrinsic physical aspect of VSBs is neglected, and the basin floor is considered flat and coplanar with the inlet and outlet channels rather than slanted as in typical VSBs. The 3-D view of the simplified geometry is depicted on the right-hand side of Figure 1. Although this simple geometry is easy to set up numerically, both in terms of grid generation and applying boundary conditions, the flow field that results is significantly more complicated due to the corners of this cubical tank.

In order to examine the OBCs and investigate the basic flow structure in this model VSB, the range of viscosity is initially chosen to keep the flow in a laminar, steady regime. This will permit a more straightforward assessment of performance of the OBC implementation without having to consider effects arising from a turbulence model. Assessment of two representative turbulence models is then presented in Section 5.

4. LAMINAR FLOW RESULTS

A 3-D general curvilinear code employing SIMPLE as the solution algorithm was developed to investigate the flow field in the VSB. This code also contains a free-surface tracking capability (using a volume of fluid, piecewise linear interface calculation due to Gueyffier *et al*. [18]), but as a first step we employed the code with a Cartesian grid, and without free-surface modelling. The code was initially validated using standard 3-D benchmarks such as laminar and turbulent duct flow and laminar lid-driven cavity flow. In this section of the paper, results from numerical simulation of laminar flow in a simplified VSB are presented. These results are used to test the OBC procedure and to interpret the flow behaviour in the cubical model VSB.

DOI: 10.1002/fld

4.1. Grid-function convergence test

Since there are no previous experimental or numerical data for this specific test case and furthermore, experimental measurement near the swirling outlet is very difficult, the calculation cannot be validated using extant results. Hence, grid-function convergence tests will be used to verify the numerical results. These tests provide an indication that the discrete equations are being solved correctly and that the numerical approximation is consistent with the analytical governing equations. To extract the order of accuracy, solutions on three different grids are required. If grid refinement is performed with constant ratio r, the observed order of accuracy q can be extracted from

$$q = \ln\left(\frac{\|f_3 - f_2\|}{\|f_2 - f_1\|}\right) \Big/ \ln r \tag{11}$$

as given by Roache [19]. Note that f_1 is the solution computed on the finest grid, and the strong L^2 norm is used to calculate solution differences used in Equation (11). Solutions were obtained on grids containing 20^3, 40^3 and 80^3 (denoted as grid 3, grid 2 and grid 1, respectively) grid cells with Reynolds number $Re = 1000$ based on the inlet channel width and inlet velocity. The power-law and QUICK schemes were used to discretize convective terms, and grid-function convergence tests were calculated for both methods individually. These results, computed in the entire domain for the velocity components and pressure, are listed in Table I. It is noteworthy that the QUICK scheme is always replaced by the power-law scheme near all boundaries. The results are fairly close to the formal order of accuracy for power-law and QUICK schemes which are first- and second-order accurate, respectively. Due to very small values of the vertical velocity component v in a major part of the domain, truncation (and possibly rounding) error may dominate computed values causing order of accuracy for v to be lower than expected for both power-law and QUICK schemes. These effects were worst at the outlet channel where this velocity component is negligible.

To avoid introducing points outside the computational domain we have to use the power-law scheme to discretize convection terms and first-order backward differencing in vorticity transport equations which decrease the order of accuracy particularly for tangential velocity components. The maximum error values for these also occur near the open channel in agreement with the previous results. Recall that by definition of vorticity, the normal velocity components also are affected at the outlet channel. Order of accuracy at the OBs can be improved by higher-order backward differencing in the vorticity definition and transport equations. Note that more refined gridding, which is hard to accomplish using a serial code, is required to achieve asymptotic convergence at the bottom outlet.

Table I. Grid-function convergence test results for entire domain.

Scheme	φ	$f_3 - f_2$	$f_2 - f_1$	$\frac{f_3 - f_2}{f_2 - f_1}$	q
Power-law	U	6.6607	3.5003	1.9029	0.9282
	V	1.1041	0.7355	1.5012	0.5861
	W	4.6287	3.2175	1.4386	0.5246
	P	6.9907	2.2640	3.0877	1.6265
QUICK	U	9.0386	1.4246	6.3447	2.6656
	V	1.8019	0.4564	3.9484	1.9813
	W	7.2625	1.1463	6.3356	2.6635
	P	10.4066	2.6289	3.9585	1.9850

DOI: 10.1002/fld

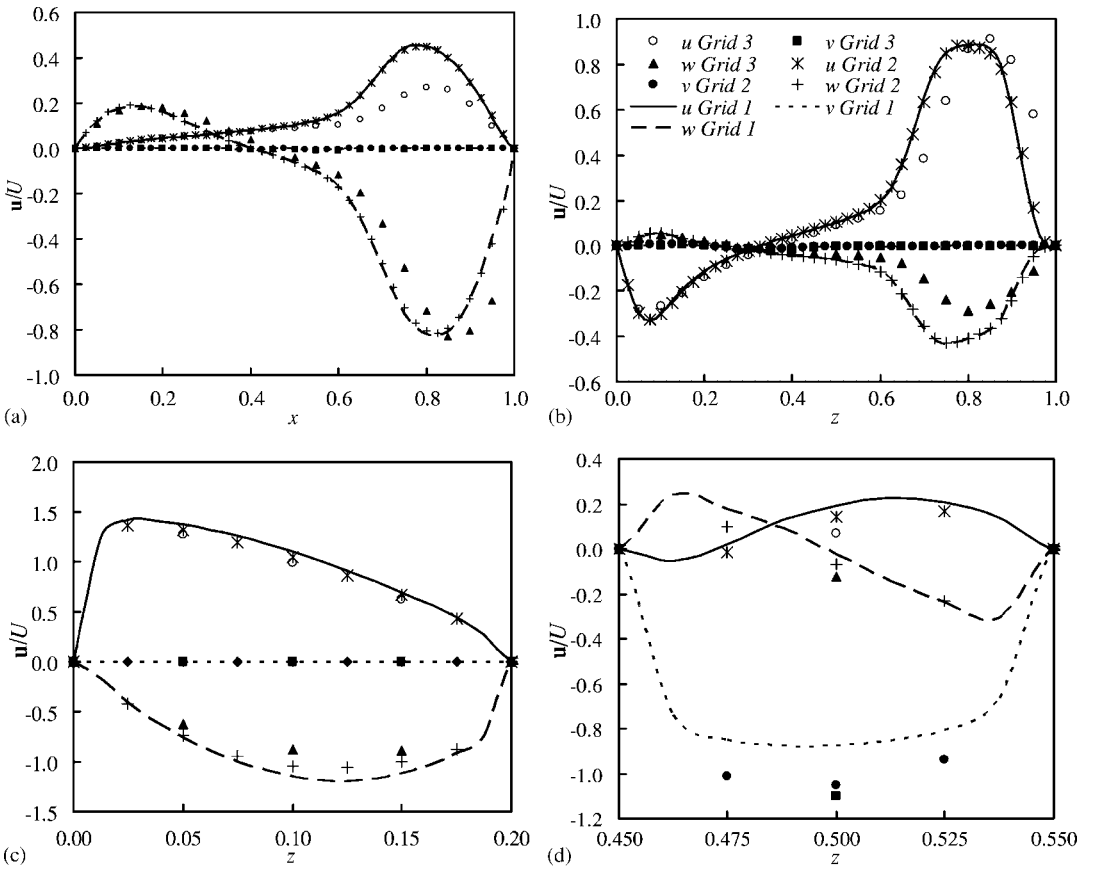

Figure 3. Velocity component profiles, computed using QUICK scheme, along lines: (a) $y = 0.5$, $z = 0.5$; (b) $x = 0.5$, $y = 0.5$; (c) $x = 1.0$, $y = 0.5$; and (d) $x = 0.5$, $y = 0.0$.

To further analyse convergence of the solutions, velocity component profiles predicted on the different grids are compared in Figure 3. Velocity profiles along the horizontal lines ($y = 0.5$, $z = 0.5$) and ($x = 0.5$, $y = 0.5$) are shown in Figures 3(a) and (b). The profiles at the outlet channel and bottom outlet are also depicted in Figures 3(c) and (d), respectively. U denotes the inlet velocity magnitude that is used to normalize the velocity components (and to define Re). Notice that with a 20^3-cell grid, there is only one point at the bottom outlet that can be used for grid-function convergence analysis, and this is not sufficient. Nevertheless, the graphs reveal that the results are converging to a grid-independent solution, and the equations are evidently being solved correctly.

4.2. Evaluation of the OBC

The velocity vectors at the bottom outlet and outlet channel calculated with an 80^3-cell grid and QUICK scheme are depicted in Figure 4. Observe that a part of the flow leaves through the bottom outlet while it is swirling (part (a)), and the other part exits the VSB after making a right-angle turn toward the outlet channel (part (b)). This demonstrates the complexity of the flow structures

DOI: 10.1002/fld

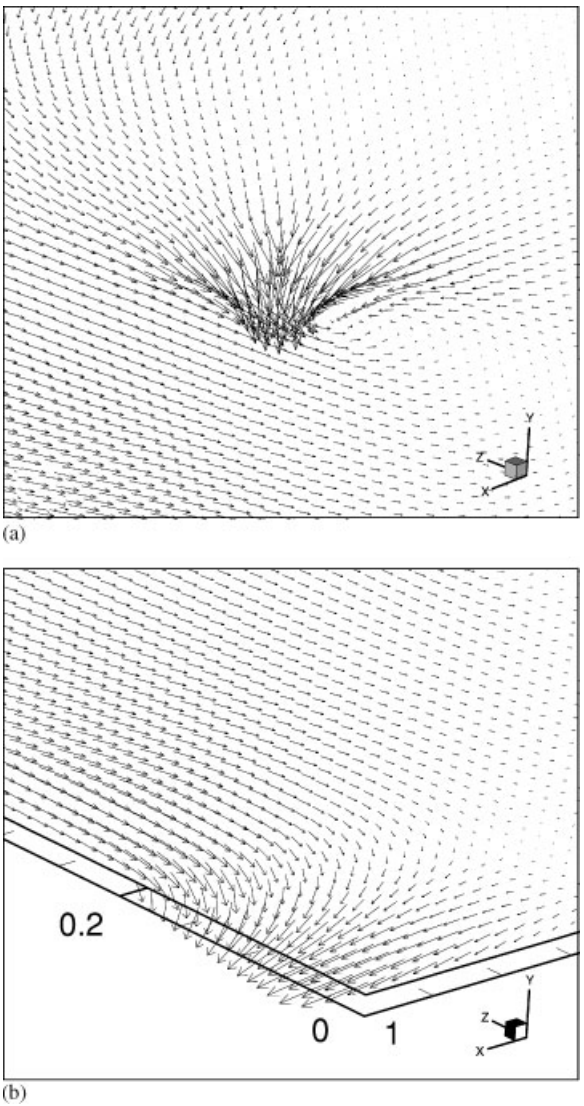

Figure 4. Velocity vectors: (a) adjacent to bottom outlet; and (b) at the outlet channel.

near the outlets. The velocity component profiles normal to these outlets are depicted in Figure 5. These profiles deviate significantly from those obtained using homogeneous Neumann boundary conditions, as is often done for such outlets. In particular, the OBC procedure can capture the normal derivative of the flow variables across the complicated OBs without any non-physical assumptions. In light of the fact, mentioned earlier, that the OBCs used here collapse to homogeneous Neumann conditions automatically in appropriate flow fields, we see from the results in Figure 5, showing significant gradients at the outlets, that the often-used fully developed flow assumption is invalid for the present case. While it must be admitted that solving momentum and vorticity equations at OB increases the amount of arithmetic, it is clear that these help to solve the complicated problem

DOI: 10.1002/fld

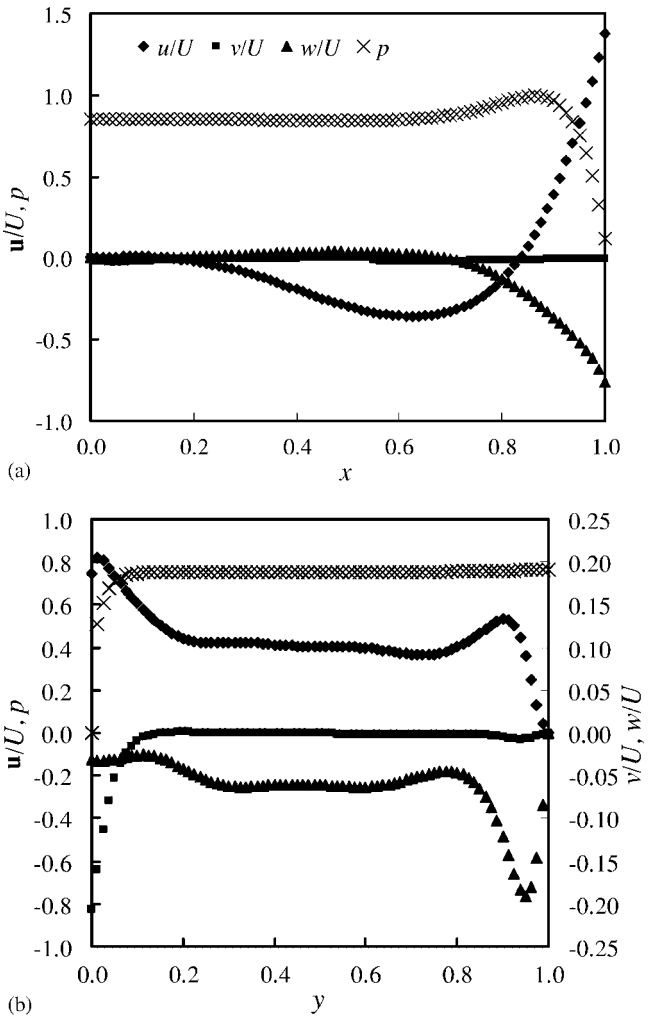

Figure 5. Flow variable profiles normal to: (a) outlet channel; and (b) bottom outlet.

in a significantly smaller domain and thus decrease the overall computational cost. Moreover, since this method allows the flow field to develop naturally, it also improves convergence to a true physical situation in comparison to homogeneous Neumann boundary conditions.

In Figure 6 velocity profiles at the OBs calculated using two different methods (see Section 2.3) to handle the normal velocity component at image points are compared. These are more distinctive at the bottom outlet (part (b) of the figure) where the flow structure is more complicated and all velocity components are effective. Notice that the method obtained by neglecting diffusion normal to the boundary and first-order upwinding is simply denoted as NR in this figure.

The volume flow rate that exits the bottom outlet is also less than 10% of the inlet flow rate in agreement with experimental results of Paul *et al*. [3]. The results reveal that by using the proposed

DOI: 10.1002/fld

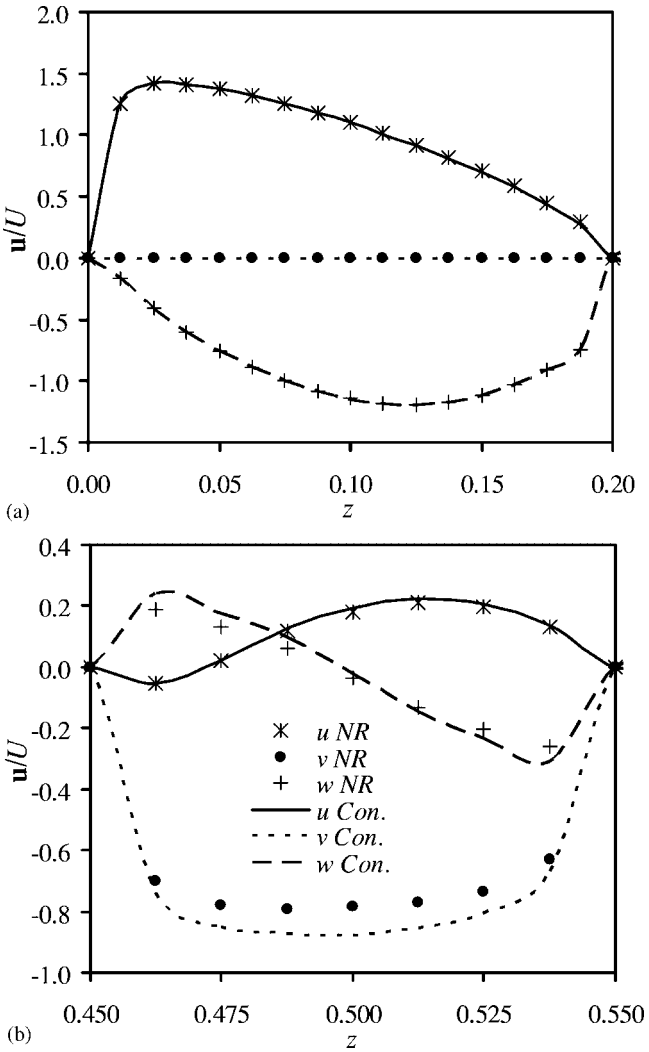

Figure 6. Comparison between velocity profiles at the outlets, computed using two different methods to handle normal velocity component at the image points.

OBC procedure, domains with multiple OBs can be simulated properly without requiring extra algorithms to split inlet flow to several OB, and without any assumptions that are made to treat the OBs in velocity–vorticity formulations [13].

4.3. Flow structure in the VSB

Although elaborate experimental studies have been carried out (e.g. [4]), flow structure in the VSB is not yet fully understood. To shed light on these flow fields, the laminar results are analysed in more detail. We remark that advanced turbulence models for 3-D computations will be needed

DOI: 10.1002/fld

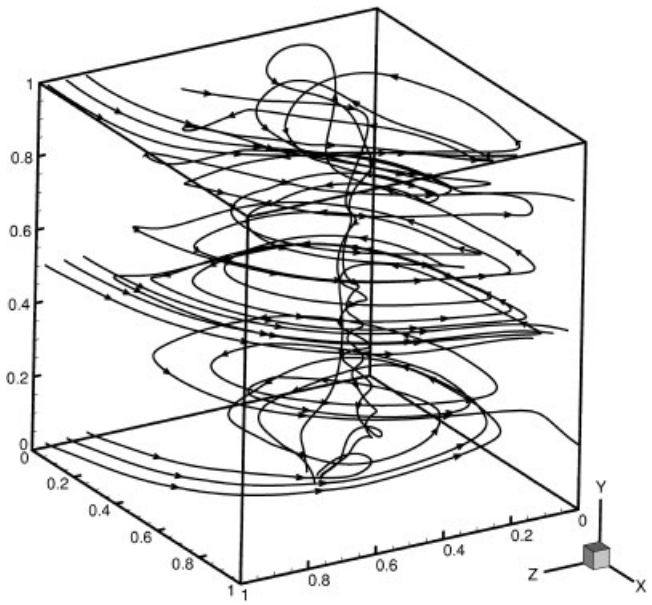

Figure 7. Trajectories of fluid particles released from various points in the vortex settling basin.

to study the complexities of high-*Re* VSB flow fields, so it is worthwhile to begin with a careful study of laminar flow that will not be contaminated by turbulence modelling effects.

To display flow trajectories, some streamlines started at the inlet are presented in Figure 7. From the computed streamlines the following complex flow pattern can be discerned: some flow from the inlet, entering mostly near mid height, goes directly to the outlet channel and exits; some streamlines follow helical paths and approach the bottom outlet, but finally exit the outlet channel. Others, initiated mainly near the bottom of the VSB, take very complicated helical paths and flush through the bottom outlet. These indicate some long paths are taken from inlet to the bottom outlet and reveal a quite complicated flow structure within the VSB, despite the fact that this is a laminar flow. Apart from corner vortices (not displayed in this figure), the flow field qualitatively resembles that in a cylindrical VSB, with a swirling flow structure near the bottom outlet as shown in this figure.

The streamlines projected on horizontal and vertical planes are depicted in Figures 8 and 9. From Figure 8 one can see that the vortex centre is displaced from the centre of the basin by generally increasing amounts as distance from the centred bottom outlet port increases. Clearly, the vortex deviates from a Rankine vortex, and the flow is not axisymmetric. Streamlines projected to the vertical x–y and y–z planes at various z and x, respectively, locations (Figure 9) display secondary flows toward the bottom outlet, particularly in Figures 9(a) and (b). Those vortices with horizontal axes would move the sediment particles from the basin periphery to the central orifice and flush them out in an actual VSB, as commented by Rea [1]. Hence, the axial velocity component v is also effective in some parts of the domain despite its generally small magnitude; and 2-D simulation cannot capture these vortices. From Figures 9(a) and (b) it can be clearly seen that the secondary flows are stronger wherever inlet and outlet channels do not influence the flow

DOI: 10.1002/fld

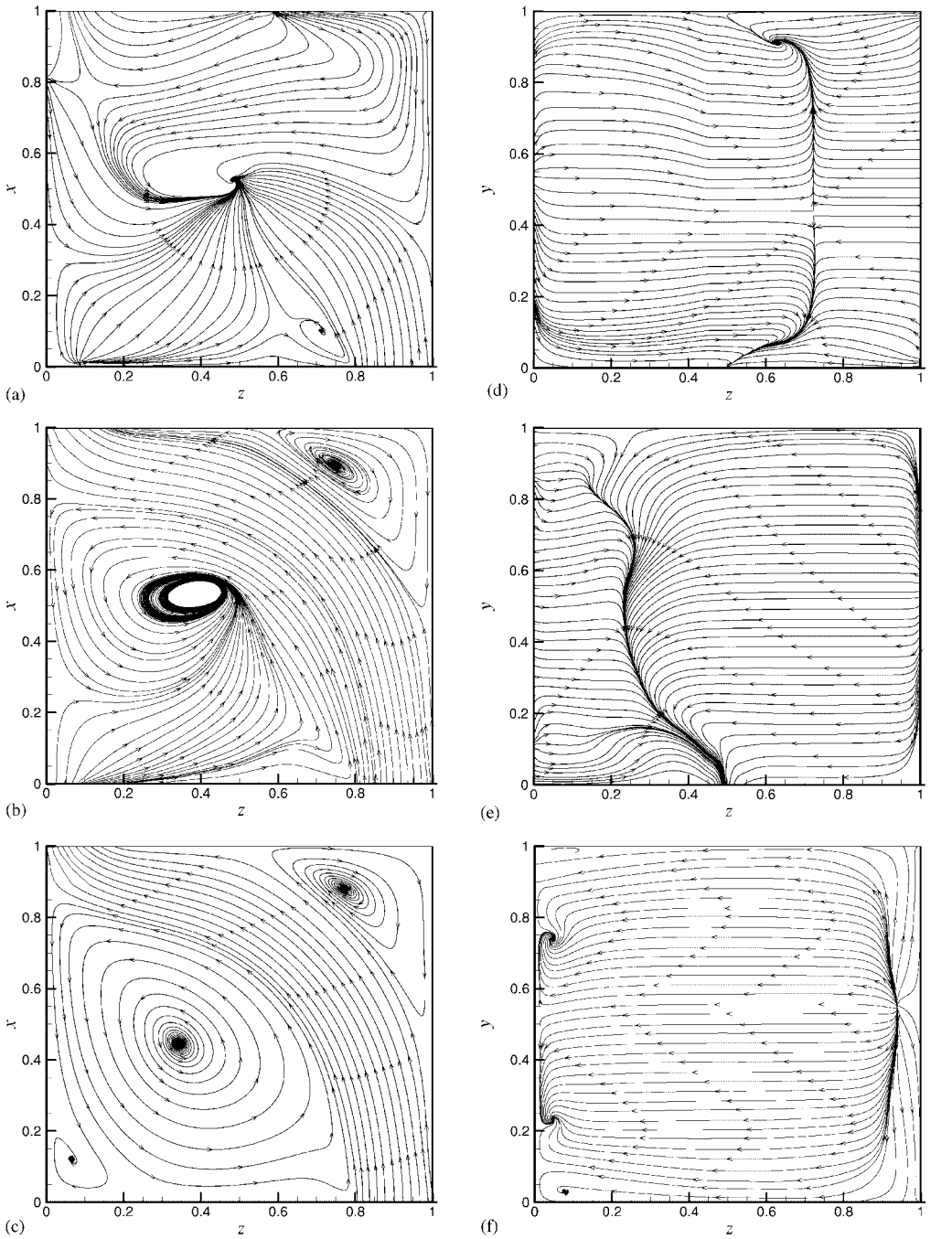

Figure 8. Streamlines projected on planes: (a) $y = 0.0125$; (b) $y = 0.0625$; (c) $y = 0.5$; (d) $x = 0.25$; (e) $x = 0.5$; and (f) $x = 0.75$.

DOI: 10.1002/fld

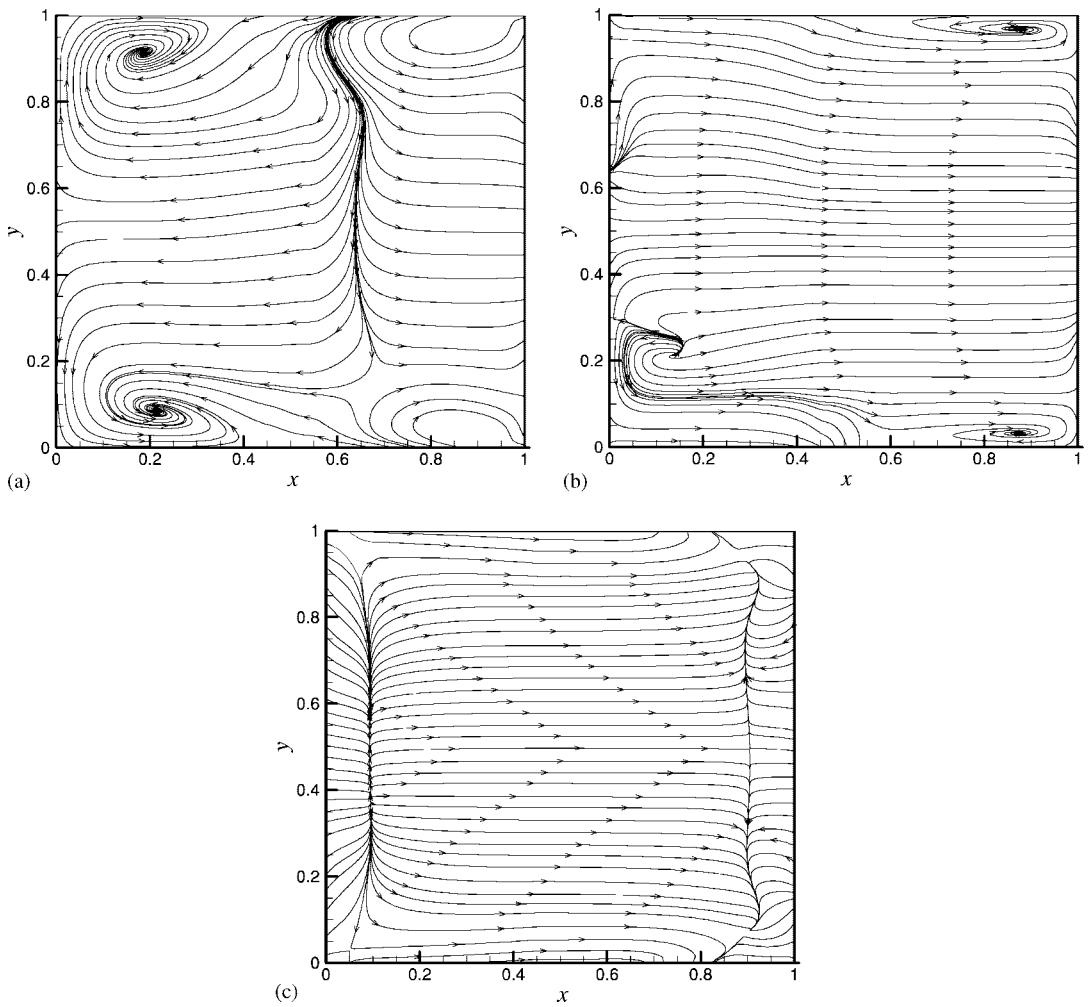

Figure 9. Streamlines projected on constant-z planes: (a) $z = 0.25$; (b) $z = 0.5$; and (c) $z = 0.75$.

pattern. In addition, Figures 8(d), (e) and (f) show no significant secondary flows in constant-x planes, with streamlines generally moving toward the central vortex, particularly near the basin floor. Observe that all streamlines adjacent to the basin floor depicted in Figure 8(a) are directed toward the bottom outlet, which supports the mentioned mechanism of sediment removal in the VSB.

Although this simulation cannot be directly compared with experimental results from an actual cylindrically shaped VSB, the values of the calculated velocities in the Cartesian coordinate system can be transformed into tangential, radial and axial velocity components to allow some qualitative comparison. Note that axial and vertical (v) velocity components are identical in the two coordinate systems, modulo effects of coupling with u and w components that differ between the coordinate systems. The velocity component profiles in horizontal planes at different distances

DOI: 10.1002/fld

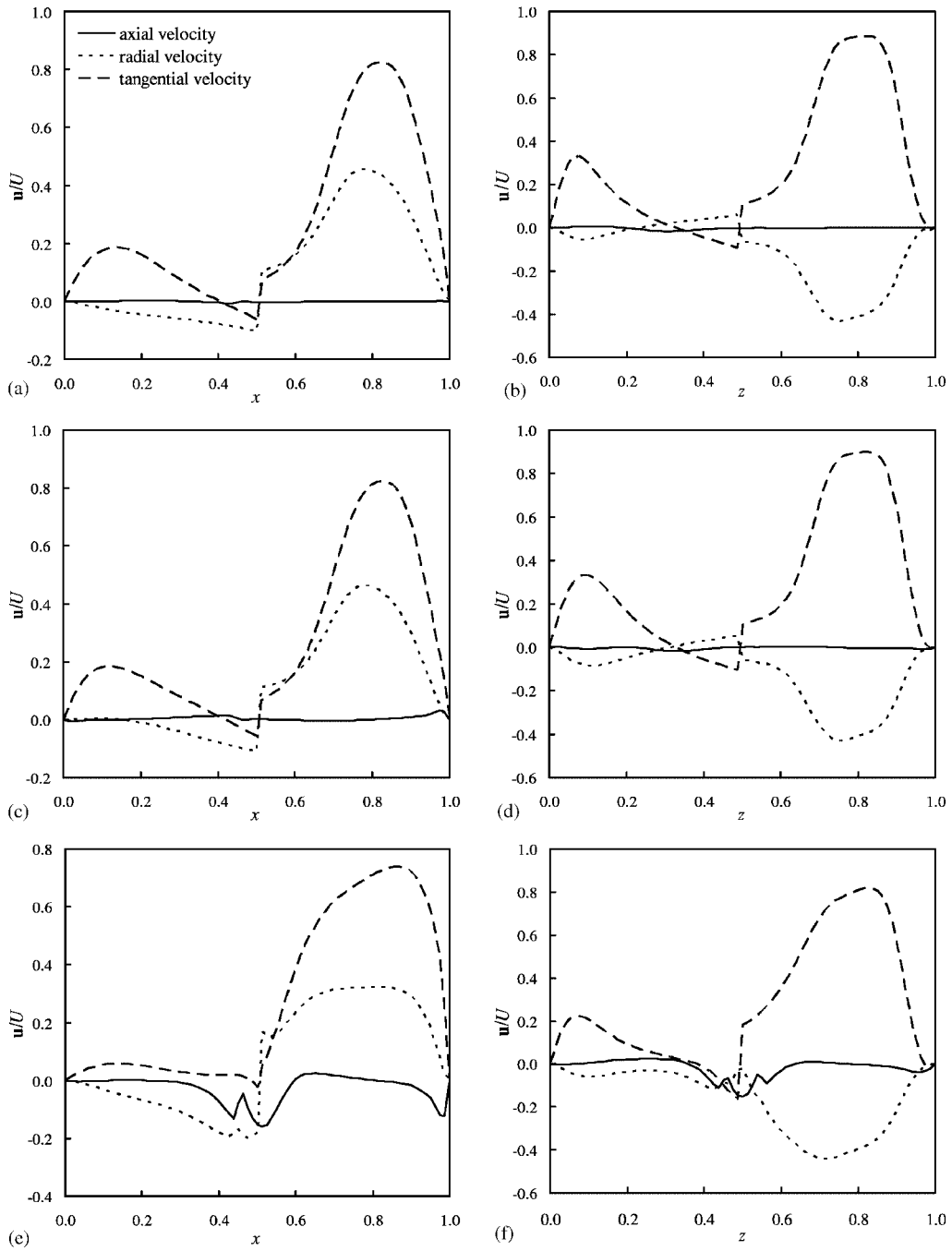

Figure 10. Velocity profiles transformed to cylindrical coordinates along lines: (a) $y = 0.5$, $z = 0.5$; (b) $x = 0.5$, $y = 0.5$; (c) $y = 0.25$, $z = 0.5$; (d) $x = 0.5$, $y = 0.25$; (e) $y = 0.0625$, $z = 0.5$; and (f) $x = 0.5$, $y = 0.0625$. Velocity profiles transformed to the cylindrical coordinates along lines: (g) $y = 0.0$, $z = 0.5$; and (h) $x = 0.5$, $y = 0.0$.

DOI: 10.1002/fld

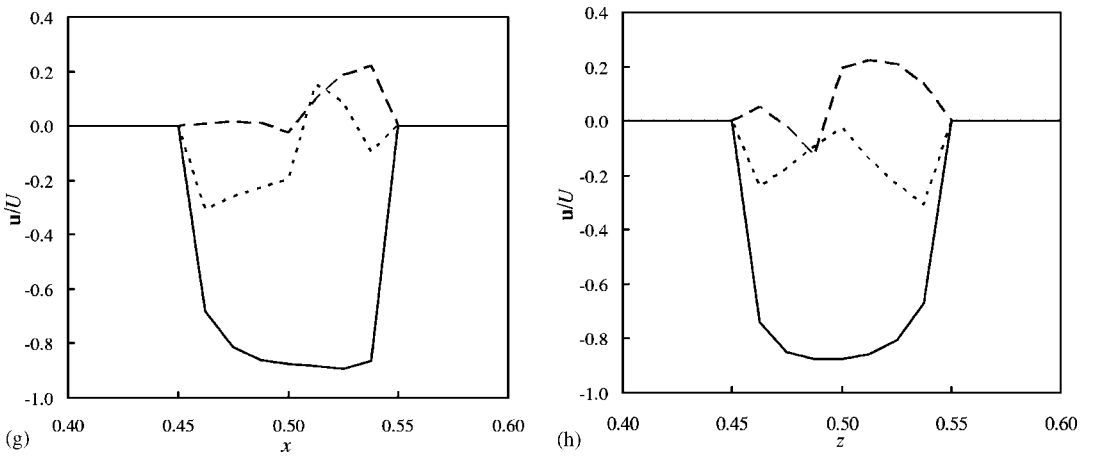

Figure 10. *Continued*.

from the bottom outlet are shown in Figure 10. The values of velocity components are calculated along two lines (viz. $x = 0.5$ and $z = 0.5$) on four horizontal cross-sections $y = 0.0$, 0.0625, 0.25 and 0.5. The tangential velocity component is dominant in the interior cross-sections. It tends to increase with increasing radius (distance from the plane centre) until it reaches two maxima at points (radius ≈ 0.32 and 0.42). At radial distances larger than those of these points, the tangential velocity decreases proportionally with radius. Due to geometry of the inlet and outlets, profiles of all velocity components have a strong asymmetrical character. The asymmetrical feature of the flow remains significant even in the bottom port where the flow leaves the basin. However, one can distinguish a forced vortex (fluid rotates as a solid body) forming around the centre and a free vortex toward the periphery that qualitatively agree with experimental results (e.g. Julien [20]). The tangential velocity decreases as the axial position approaches the bottom of the basin, and the axial velocity increases gradually toward the bottom outlet. These variations are qualitatively supported by experimental and computational studies in a hydrocyclone [11]. Although the tangential velocity decreases rapidly near the bottom outlet, the radial velocity does not change significantly, revealing the contribution of the radial velocity near the basin floor in flushing discharge through bottom outlet shown in experimental studies [3].

5. TURBULENCE MODELLING

Although weaknesses of the Reynolds-averaged Navier–Stokes (RANS) equations have been recognized since long ago, they are still in use because of lower computational cost in comparison to large-eddy simulation (LES) or direct numerical simulation (DNS) for practical problems. DNS is really far away from practical use, but LES possesses some desirable features, and it is now the subject of much active research. However, LES is still not sufficiently inexpensive for most practical flow calculations, and it also suffers from some shortcomings similar to those of RANS models.

Here performance of two widely used high-Reynolds number two-equation RANS models, the standard k–ε method of Launder and Spalding [21] and the k–ω model due to Wilcox [22], are

DOI: 10.1002/fld

studied to calculate turbulent flow in the VSB. The RANS equations are as follows:

$$\frac{\partial(\rho\mathbf{u})}{\partial t} + \nabla \cdot (\rho\mathbf{u}\mathbf{u}) = -\nabla p + (\mu + \mu_{\mathrm{T}})\Delta\mathbf{u} \tag{12}$$

$$\nabla \cdot \mathbf{u} = 0 \tag{13}$$

where $\mathbf{u}$ is now the time-averaged velocity vector $(u, v, w)^{\mathrm{T}}$, ρ is constant fluid density, p is time-averaged pressure, μ is fluid viscosity and μ_{T} is turbulent eddy viscosity. The eddy viscosity is the only term that must be modelled.

5.1. k–ε model

In the standard k–ε model, eddy viscosity is calculated as

$$\mu_{\mathrm{T}} = \rho C_{\mu} \frac{k^2}{\varepsilon} \tag{14}$$

where k is the turbulence kinetic energy, ε is the dissipation rate and C_{μ} is a model constant that must be assigned somewhat arbitrarily. The transport equations for k and ε are

$$\frac{\partial(\rho k)}{\partial t} + \nabla \cdot (\rho\mathbf{u}k) = \left(\mu + \frac{\mu_{\mathrm{T}}}{\sigma_k}\right)\Delta k + G - \rho\varepsilon \tag{15}$$

$$\frac{\partial(\rho\varepsilon)}{\partial t} + \nabla \cdot (\rho\mathbf{u}\varepsilon) = \left(\mu + \frac{\mu_{\mathrm{T}}}{\sigma_{\varepsilon}}\right)\Delta\varepsilon + C_{\varepsilon 1}\frac{\varepsilon}{k}G - C_{\varepsilon 2}\rho\frac{\varepsilon^2}{k} \tag{16}$$

where $G = \mu_{\mathrm{T}}(\nabla\mathbf{u} + (\nabla\mathbf{u})^{\mathrm{T}}) : \nabla\mathbf{u}$ is the production of turbulence kinetic energy and : denotes tensor scalar product. The model closure coefficients employed here are the 'standard' ones (see, e.g. Wilcox [23]): $C_{\mu} = 0.09$, $\sigma_k = 1.0$, $\sigma_{\varepsilon} = 1.3$, $C_{\varepsilon 1} = 1.44$ and $C_{\varepsilon 2} = 1.92$.

5.2. k–ω model

In the k–ω model, eddy viscosity is obtained from

$$\mu_{\mathrm{T}} = \rho\frac{k}{\omega} \tag{17}$$

where k is again the turbulence kinetic energy and ω is the specific dissipation rate (the rate of dissipation per unit turbulence kinetic energy). The transport equations for k and ω are:

$$\frac{\partial(\rho k)}{\partial t} + \nabla \cdot (\rho\mathbf{u}k) = (\mu + \sigma^*\mu_{\mathrm{T}})\Delta k + G - \beta^*\rho k\omega \tag{18}$$

$$\frac{\partial(\rho\omega)}{\partial t} + \nabla \cdot (\rho\mathbf{u}\omega) = (\mu + \sigma\mu_{\mathrm{T}})\Delta\omega + \alpha\frac{\omega}{k}G - \beta\rho\omega^2 \tag{19}$$

The model closure coefficients are: $\alpha = \frac{5}{9}$, $\beta = \frac{3}{40}$, $\beta^* = 0.09$, $\sigma = 0.5$ and $\sigma^* = 0.5$.

DOI: 10.1002/fld

5.3. Wall function

The walls of the VSB are treated as no-slip surfaces, and wall shear stress, turbulence kinetic energy and dissipation rate adjacent to the wall are calculated based on a wall function, as is rather standard. The simplified form of the two-layer Cheing and Launder [24] model is adopted to define the wall function for the present study. In this model the wall shear stress is evaluated as in a standard wall function. Then the wall layer is divided into a viscous sublayer and a turbulent outer region based on values of y^+ defined here as

$$y^+ = \frac{\rho C_\mu^{0.25} k^{0.5} y}{\mu} \tag{20}$$

where y is distance from the wall. For the average production in the fully turbulent region ($y^+ > 11.22$) the turbulent shear stress is assumed to be constant and equal to the wall shear stress, while in the viscous sublayer the turbulent stress is assumed to be zero. The average dissipation rate is obtained by assuming ε to be constant in the viscous sublayer and equal to its wall limiting value, such that k increases quadratically across the viscous sublayer. In the turbulent region ε varies according to the equilibrium length scale, and the turbulence kinetic energy is assumed to be constant outside the sublayer. This model was chosen due to its non-equilibrium feature of improved behaviour near solid walls in complicated geometries such as those of the VSB, especially near inlets and outlets, where standard wall function assumptions are violated.

5.4. Turbulence properties at the OBs

Non-reflecting boundary conditions have been used in the extant literature (e.g. Wu [25]) to deal with turbulence properties (k, ε and ω) at the OBs. Here we solve the transport equation for these properties at OBs. To avoid introduction of properties outside the computational domain, the diffusion term normal to the OBs, production and dissipation terms are all neglected, and a first-order upwind scheme is used to treat convective terms. The resulting equations resemble usual non-reflecting boundary conditions. However, these include the diffusion and convection terms in tangential directions in the present case. To define turbulence properties, fully developed duct flow is assumed at the inlet.

5.5. Turbulence modelling results

The RANS equations are discretized using the same approach as employed for laminar flow. However, the power-law scheme is used uniformly to treat convection terms in turbulence property transport equations, and all scalar turbulence quantities are evaluated at cell centres. All computations to be presented here have been carried out at $Re = 10^5$, a typical value for VSB operation.

The streamlines predicted on a 40^3-cell grid using the k–ω model are plotted in Figure 11, and streamlines projected onto horizontal and vertical planes are depicted in Figures 12 and 13, respectively. Due to assumptions buried in the turbulence models, the predicted flow field is far simpler than that of laminar flow at much lower Re (compare Figure 11 with Figure 7). The flow is almost axisymmetric, and few secondary flows are observed due to massive numerical diffusion arising from use of the Boussinesq hypothesis. As pointed out by Wilcox [23], all models based on this hypothesis fail when flow experiences extra rate of strain caused by streamline curvature and numerous other effects of 3-D flows. The implemented wall function also cannot predict streamline

DOI: 10.1002/fld

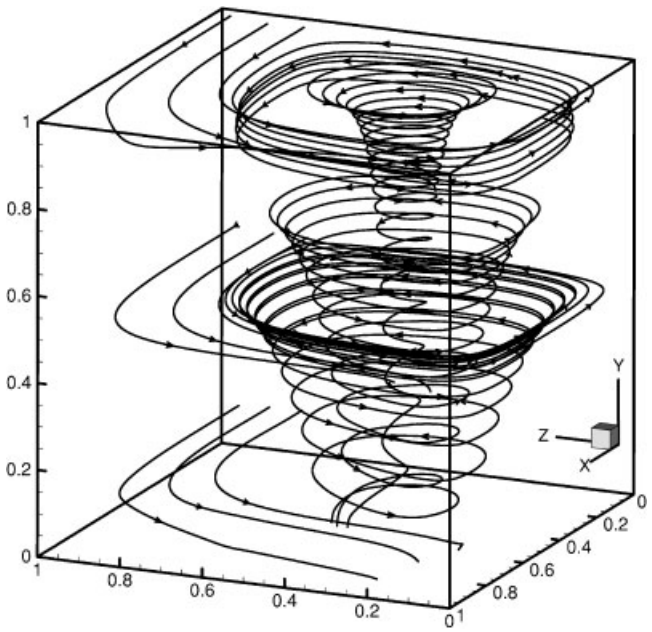

Figure 11. Some predicted streamlines started from inlet in the vortex settling basin using k–ω model.

curvature and adverse pressure gradients of corner vortices. However, these discrepancies can be circumvented to some extent by adding streamline curvature effects to the turbulence models. Using more general wall functions (e.g. Craft *et al*. [26]) might also enhance the results to some extent.

The flow structure near the outlets is shown in Figure 14. This figure shows the expected swirling flow at the bottom outlet. The predicted flow structures near the outlets are generally similar to the laminar case, and normal derivatives of velocity and pressure at these OBs are not zero. The transformed velocity components of cylindrical coordinates are depicted in Figure 15. These profiles clearly show the steep velocity gradient near the walls. There is also evidence of free and forced vortex formation, but it is not as obvious as in the laminar flow. We note that predicted velocity components obtained using the two turbulence models are essentially identical. In particular, for this problem there appears to be no reason to prefer one over the other (but see below).

Contour plots of turbulence properties are shown in Figures 16 and 17 corresponding to use of k–ω and k–ε models, respectively. These values are normalized by inlet velocity, fluid density and viscosity as: $k = k^*/U^2$, $\varepsilon = \mu\varepsilon^*/\rho U^4$, $\omega = \mu\omega^*/\rho U^2$, where * superscripts denote dimensional parameters. The maximum values of these quantities occur near the outlets, adjacent to the inlet and somewhat generally near solid boundaries. Steep velocity gradients (not displayed here) near the solid boundaries and at the outlet channel are observable, consistent with high values of the turbulence quantities seen at these locations. But the highest values of these occur, rather unexpectedly, at the inlet. In general, the two models produce qualitatively similar results for turbulence kinetic energy, which can be directly compared between Figures 16(a) and 17(a); but

DOI: 10.1002/fld

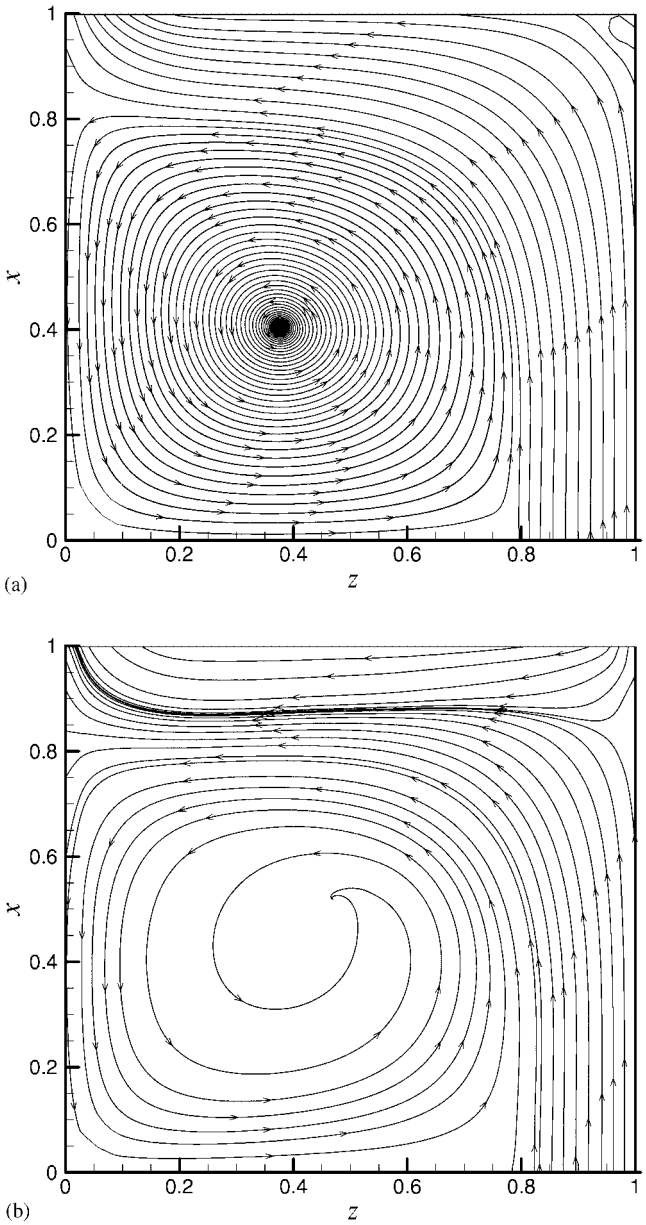

Figure 12. Streamlines projected on horizontal planes: (a) $y = 0.5$ and (b) $y = 0.025$, predicted using k–ω model.

DOI: 10.1002/fld

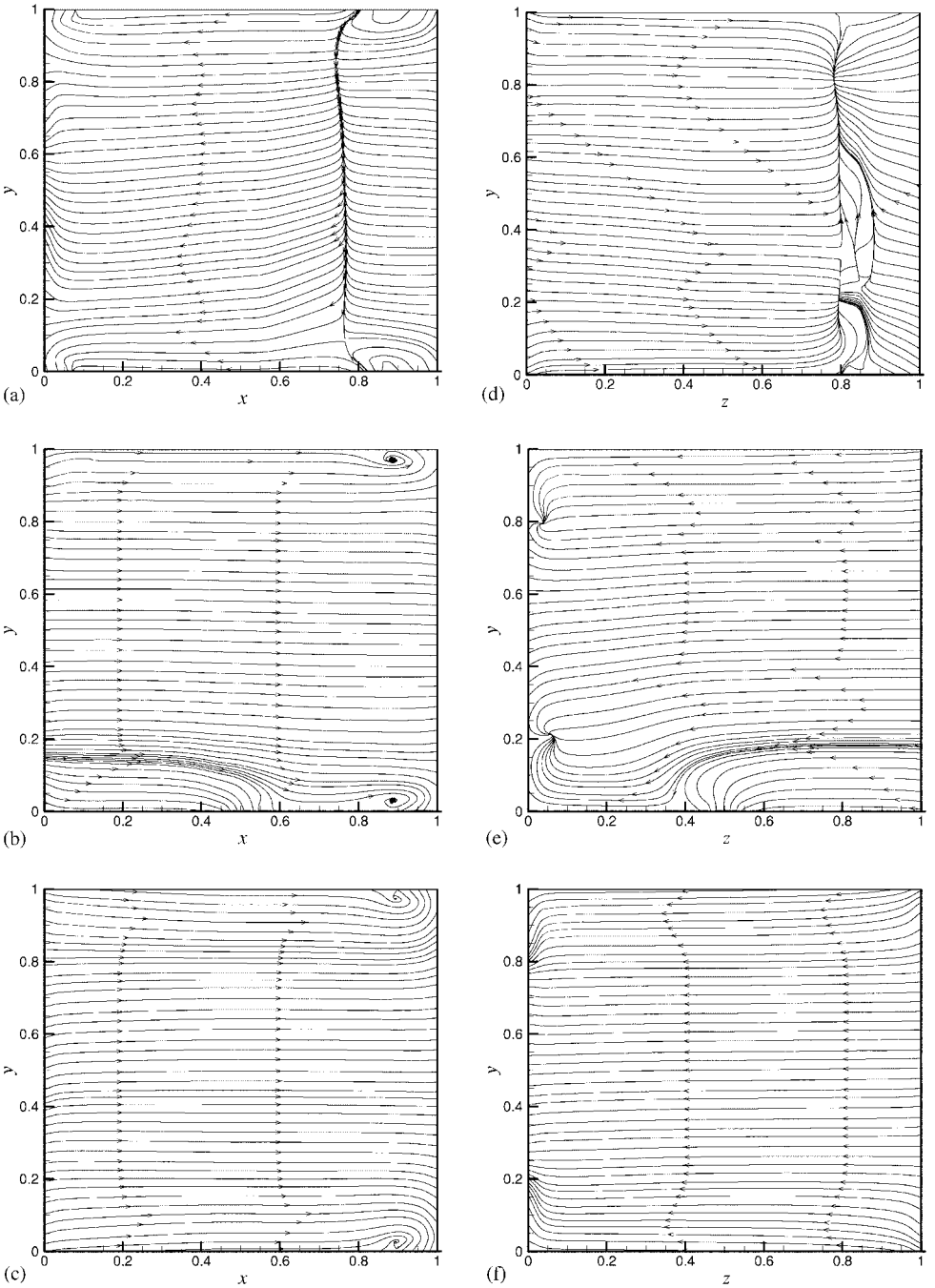

Figure 13. Streamlines projected on vertical planes: (a) $z = 0.25$; (b) $z = 0.5$; (c) $z = 0.75$; (d) $x = 0.25$; (e) $x = 0.5$; and (f) $x = 0.75$, predicted using k–ω model.

DOI: 10.1002/fld

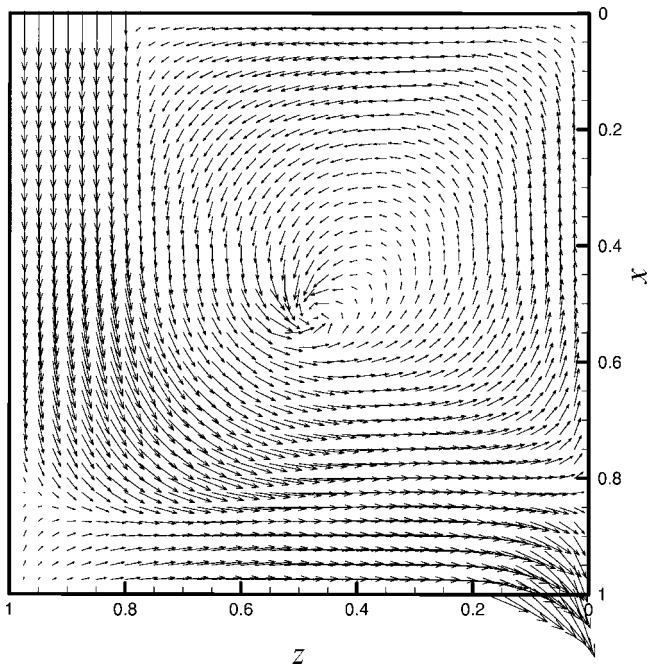

Figure 14. Velocity vector at open boundaries computed using k–ω model.

that from the k–ω model is approximately double that of the k–ε model. We must emphasize, however, that no adjustment from standard values has been made in closure constants for either case; in particular, we have not as yet investigated whether these discrepancies can be reconciled. Moreover, as noted earlier, there are not yet any experimental results available for this simplified model to provide an absolute assessment of model strengths and deficiencies.

6. SUMMARY, CONCLUSIONS AND FUTURE WORK

In this paper a method to set boundary conditions at OB has been presented. This method allows us to solve the 3-D incompressible N.–S. equations in a primitive-variable formulation in geometrically complicated domains without employing any non-physical assumptions at outlets. Multiple OBs can be simulated with no need to provide an extra algorithm for splitting the inlet flow rate among several OBs. The method was implemented to treat two complicated OBs in a simplified VSB for both laminar and turbulent flow regimes.

It was inferred from computed results that homogeneous Neumann boundary conditions cannot correctly represent the flow structures at VSB outlets. The complicated laminar flow structure in the VSB was analysed in detail, and preliminary assessment of two popular turbulence models was made. These two-equation models could not properly simulate the flow field in the VSB due to their dependence on the Boussinesq hypothesis, although they might be improved by adding streamline curvature effects; and they should be calibrated using experimental data. Finally we note

DOI: 10.1002/fld

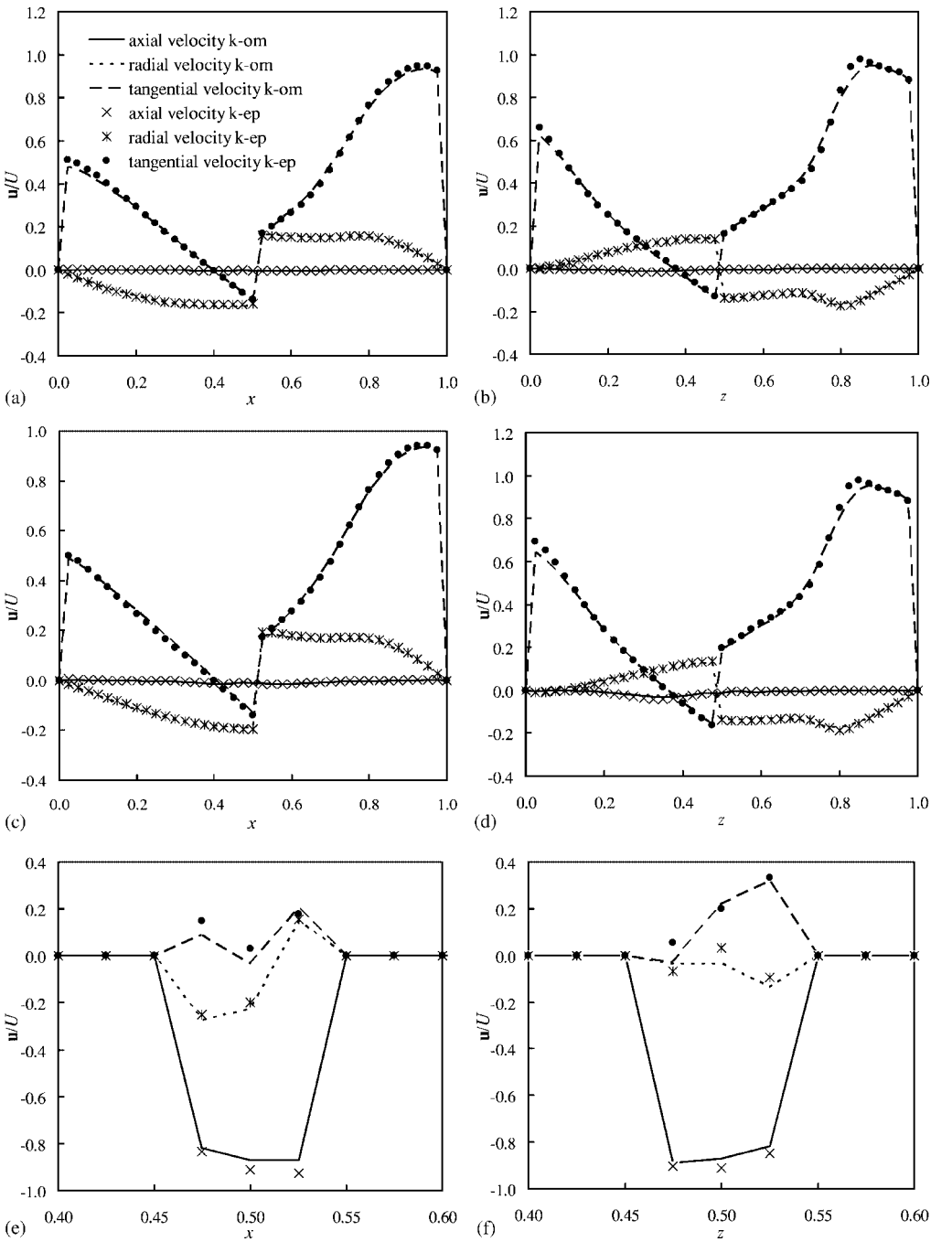

Figure 15. The turbulent velocity profiles transformed to cylindrical coordinates along: (a) $y=0.5$, $z=0.5$; (b) $x=0.5$, $y=0.5$; (c) $y=0.25$, $z=0.5$; (d) $x=0.5$, $y=0.25$; (e) $y=0.0$, $z=0.5$; and (f) $x=0.5$, $y=0.0$.

DOI: 10.1002/fld

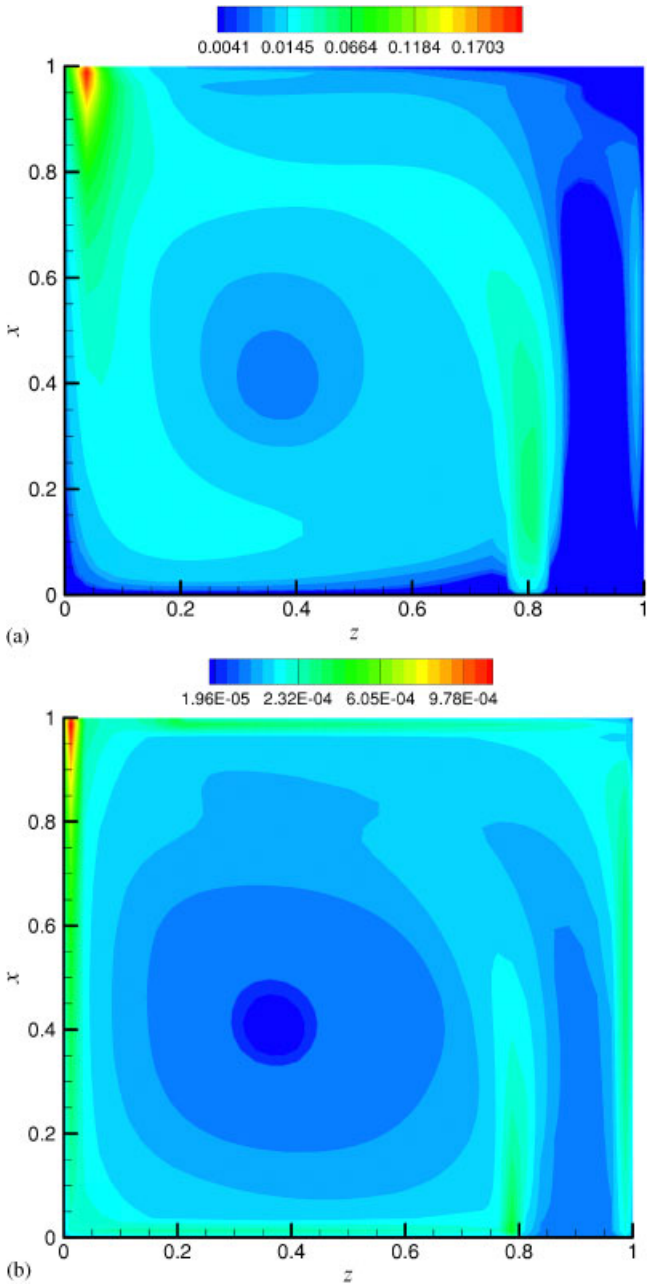

Figure 16. Contour plots of: (a) k and (b) ω on plane $y = 0.5$ computed using k–ω model.

DOI: 10.1002/fld

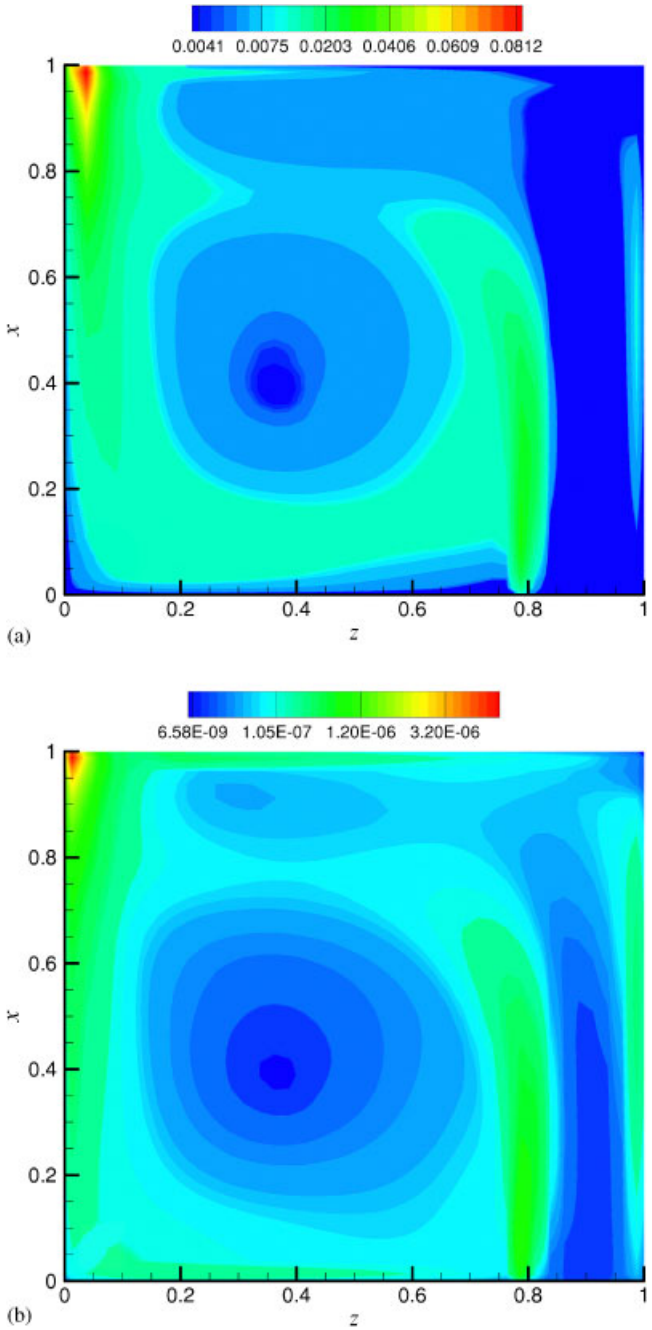

Figure 17. Contour plots of: (a) k and (b) ε on plane $y = 0.5$ computed using k–ε model.

DOI: 10.1002/fld

that free-surface and turbulence modelling in general curvilinear coordinate systems are required to simulate an actual VSB flow structure, and this will be the focus of future efforts.

ACKNOWLEDGEMENTS

The first author was supported by Shiraz University, Shiraz Iran, for a short visiting research period at the University of Kentucky. He also received partial support from University of Kentucky Center for Computational Sciences. We thank the University of Kentucky Computing Center for providing access to the HP SuperDome SMP for all computations reported herein.

REFERENCES

1. Rea Q. Secondary currents within the circulation chamber sediment extractor. *M.S. Thesis*, University of Southampton, Southampton, U.K., 1984.
2. Athar M, Kothyari UC, Garde RJ. Distribution of sediment concentration in the vortex chamber type sediment extractor. *Journal of Hydraulic Research* 2003; **41**(4):427–438.
3. Paul TC, Sayal SK, Sakhanja VS, Dhillon GS. Vortex settling basin design considerations. *Journal of Hydraulic Engineering* 1991; **117**(2):172–189.
4. Athar M, Kothyari UC, Garde RJ. Sediment removal efficiency of vortex chamber type sediment extractor. *Journal of Hydraulic Engineering* 2002; **128**(12):1051–1059.
5. Nowakowski AF, Cullivan JC, Williams RA, Dyakowski T. Application of CFD to modeling of the flow in hydrocyclone. *Minerals Engineering* 2004; **17**:661–669.
6. Sani RL, Gresho PM. Resume and remarks on the open boundary condition mini-symposium. *International Journal for Numerical Methods in Fluids* 1994; **18**:983–1008.
7. Gresho PM. Incompressible fluid dynamics: some fundamental formulation issues. *Annual Review of Fluid Mechanics* 1991; **23**:413–453.
8. Shyy W. Numerical outflow boundary conditions for Navier–Stokes flow calculation by a line iterative method. *AIAA Journal* 1985; **23**:1847–1848.
9. Behr M, Liou J, Shih R, Tezduyar TE. Vorticity-streamfunction formulation of unsteady incompressible flow past a cylinder: sensitivity of the computed flow field to the location of the outflow boundary. *International Journal for Numerical Methods in Fluids* 1991; **12**:323–342.
10. Concha F, Barrientos A, Montero J, Sampaio R. Air core and roping in hydrocyclones. *International Journal of Mineral Processing* 1996; **44–45**:743–749.
11. Nowakowski AF, Dyakowski T. Investigation of swirling flow structure in hydrocyclones. *Trans. IChem.E, Part A, Chem. Eng., Res. Des.* 2003; **81**(A8):862–873.
12. Doby MJ, Kraipech W, Nowakowski AF. Numerical prediction of outlet velocity patterns in solid–liquid separators. *Chemical Engineering Journal* 2005; **11**:173–180.
13. Bertagnolio F. Solution of the incompressible Navier–Stokes equations on domains with one or several open boundaries. *International Journal for Numerical Methods in Fluids* 1999; **31**:1061–1085.
14. Liu CH. Numerical solution of 3-D Navier–Stokes equations by a velocity–vorticity method. *International Journal for Numerical Methods in Fluids* 2001; **35**:533–557.
15. Patankar SV. *Numerical Heat Transfer and Fluid Flow*. McGraw-Hill: New York, 1980.
16. Chrysostomou V. Vortex-type settling basin. *M.S. Thesis*, University of Southampton, Southampton, U.K., 1983.
17. Ziaei AN. Study on the efficiency of vortex settling basin (VSB) by physical modeling. *M.S. Thesis*, Shiraz University, Shiraz, Iran, 2000.
18. Gueyffier D, Li J, Nadim A, Scardovelli R, Zaleski S. Volume-of-fluid interface tracking with smoothed surface stress methods for 3-D flows. *Journal of Computational Physics* 1999; **152**:423–456.
19. Roache PJ. Verification of codes and calculations. *AIAA Journal* 1998; **36**(5):696–702.
20. Julien PY. Concentration of very fine silts in a steady vortex. *Journal of Hydraulic Research* 1986; **24**(4):255–264.
21. Launder BE, Spalding DB. The numerical computation of turbulent flows. *Computer Methods in Applied Mechanics and Engineering* 1974; **3**:269–289.
22. Wilcox DC. Reassessment of the scale determining equations for advanced turbulence models. *AIAA Journal* 1988; **26**:1299–1310.

DOI: 10.1002/fld

23. Wilcox DC. *Turbulence modeling for CFD*. DCW Industries, Inc.: La Canada, CA, 1993.
24. Chieng CC, Launder BE. On the calculation of turbulent heat transport downstream from an abrupt pipe expansion. *Numerical Heat Transfer* 1980; **3**:189–207.
25. Wu, TR. A Numerical study of 3-D break waves and turbulence effects. *Ph.D. Thesis*, Cornell University, Ithaca, NY, 2004.
26. Craft TJ, Gerasimov AV, Iacovides H, Launder BE. Progress in the generalization of wall function treatments. *International Journal of Heat and Fluid Flows* 2002; **23**:148–160.

DOI: 10.1002/fld